Thermal analysis of fault-tolerant electrical machines for aerospace actuators

Vincenzo Madonna [1*], Paolo Giangrande [1], Chris Gerada[1,2], Michael Galea [1,2]

[1] PEMC Group, University of Nottingham, Nottingham, NG7 2RD, UK
[2] School of Aerospace, University of Nottingham Ningbo China, Ningbo 315100, China
[*]Vincenzo.Madonna2@nottingham.ac.uk

Abstract: For safety critical applications, electrical machines need to satisfy several constraints, in order to be considered fault-tolerant. In fact, if specific design choices and appropriate control strategies are embraced, fault-tolerant machines can operate safely even in faulty conditions. However, particular care should be taken for avoiding uncontrolled thermal overload, which can either cause severe failures or simply shorten the machine lifetime. This paper describes the thermal modelling of two permanent magnet synchronous machines for aerospace applications. In terms of the winding's layout, both machines employ concentrated windings at alternated teeth, with the purpose of accomplishing fault tolerance features. The first machine (i.e. *Machine A*) adopts a three-phase winding configuration, while a double three-phase configuration is used by the second one (i.e. *Machine B*). For both machines, the winding temperatures are evaluated via simplified thermal models, which were experimentally validated. Copper and iron losses, necessary for the thermal simulations, are calculated analytically and through electromagnetic finite element analysis respectively. Finally, two aerospace study cases are presented, and the machines' thermal behaviour is analysed during both healthy and faulty conditions. Single-phase open-circuit and three-phase short-circuit are accounted for *Machine A* and *B* respectively.

1. Introduction

In traditional fuel-powered aircraft, the main task of the engines consists in producing propulsive power by converting the energy stored in the fuel. A percentage of the fuel energy also serves for generating non-propulsive power, namely pneumatic, hydraulic, mechanical and electric [1, 2]. At the beginning of 1990s, the More Electric Aircraft (MEA) concept was proposed by the US Air Force. The MEA initiative promotes the use of electric power on-board aircraft, in place of pneumatic, hydraulic and mechanical powers [3-5]. Electrical machines play a significant role on aircraft that endorse the MEA concept. Indeed, they are used in several applications, such as for driving valves, actuators, pumps, fans etc. [6, 7]. Nevertheless, electrical machines for aerospace applications should be characterised by great power density, high reliability and fault-tolerance capability [8-10]. A machine topology able to satisfy high power density requirement is the permanent magnet synchronous machine (PMSM). However, the presence of permanent magnets (PMs) is a source of concern. Since the excitation field is constantly present, then the machine is always 'on'. In PMSMs, a suitable fault-tolerance level is achieved when the following constraints are met [11, 12]:

a. Physical separation between phases;
b. Magnetic isolation between phases;
c. Implicit limiting of fault currents;
d. Effective thermal isolation between phases;
e. Complete electrical isolation between phases.

Conditions *a-c* are simultaneously satisfied by adopting a concentrated winding at alternated teeth (CW-AT) as winding layout. Due to the coils arrangement, the CW-AT configuration ensures physical isolation among the phases. Further, the CW-AT pattern leads to a high per-unit self-inductance and negligible mutual inductance, which confine the current value in the occurrence of fault [13, 14]. Since each slot contains only coils belonging to the same phase, condition *d* is also fulfilled [15].

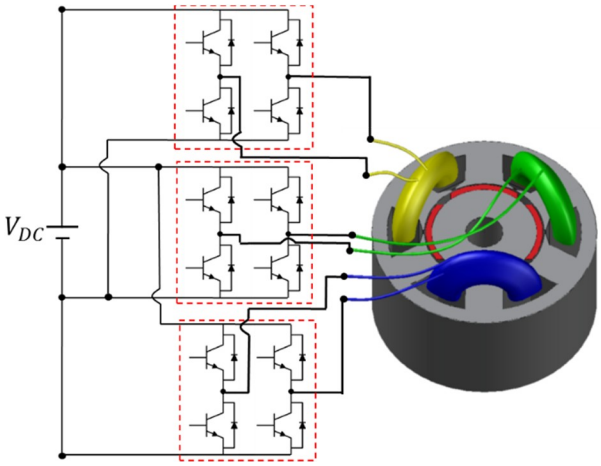

***Fig. 1**. Example of fault-tolerant three-phase CW-AT PMSM drive.*

Condition *e* is usually very difficult to reach, mainly because it being inherently a system-level issue. It can be met by using independent power supplies either for each machine phase [16] or for each winding set, like in double three-phase machines [7]. This approach, known as power segmentation, allows for a true electrical isolation between phases; thus, the machine is able to operate also under extreme fault conditions, such as open- and short-circuits [17, 18]. Fig. 1 shows an example of a three-phase fault-tolerant PMSM drive, while an illustration of double three-phase fault-tolerant PMSM drive is sketched in Fig. 2. Both configurations implement CW-AT windings and power segmentation. In case of open- or short-circuit faults, PMSMs can still deliver the required torque by applying appropriate control strategies. Generally, these correction

strategies aim to increase the current in the healthy phases. For this reason, particular care must be taken in order to avoid uncontrolled thermal overload, which may trigger critical damage (e.g. PM demagnetisation, windings insulation breakdown, etc...) leading to drive downtime. Further, thermal overload might drastically compromise the insulation system lifetime, since as a rule of thumb, a 10°C increase in winding temperature halves the insulation lifetime [19, 20].

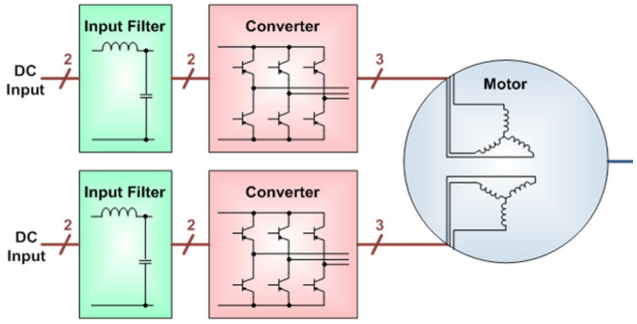

Fig. 2: *Example of double three-phase fault-tolerant PMSM drive.*

Hence, the machine thermal analysis is necessary for both healthy and faulty conditions. Such analysis can be carried out by building a Lumped Parameter Thermal Network (LPTN) of the machine under study [21]. The LPTN provides accurate temperature estimation with low computational time [22].

This paper focuses on the thermal behaviour of fault-tolerant PMSMs for aerospace applications. The considered machines are investigated in both healthy and fault conditions. In particular, the three-phase machine (defined hereafter *Machine A*) is thermally analysed during single-phase open-circuit fault. Conversely, the thermal analysis of the double three-phase machine (defined hereafter *Machine B*) is performed with one set of three-phase winding short-circuited. Experimentally validated LPTNs are utilized for evaluating the winding temperatures. The PMSMs design and their LPTNs are discussed, along with the LPTNs building procedure. Experimental results are then used to validate the predicted LPTNs outcomes.

2. PMSMs parameters and applications

2.1. Machine A

The fault-tolerant PMSM, defined as *Machine A,* is a 30 slots and 28 poles machine, adopting a three-phase CW-AT arrangement. Thus, each slot contains only one coil's side. This PMSM is designed for a flap control Electro Mechanical Actuator (EMA) installed on a medium sized civil aircraft (e.g. B737 or A320). A simplified diagram of the application, based on the architecture described in [23], is reported in Fig. 3. At the actuator pivot, a torque of about 30 kNm is needed. Due to the high torque demanded, a mechanical gearbox is placed between the actuator pivot and the PMSM shaft. Indeed, the designed PMSM develops 130 Nm at 350 rpm, since a gearbox with 290:1 step-down ratio and 80% efficiency is mounted on the drivetrain.

Table 1 lists the main design parameters of *Machine A*, while Fig. 4 shows the geometry and the winding layout.

Table 1 PMSMs parameters

Parameter	Machine A	Machine B
Slot number (Q)	30	12
Pole pairs (p)	14	5
Rated Current (In)	28.3 Arms	2.2 Arms
Stack length (L)	130 mm	136.5 mm
Stator outer diameter (D_e)	250 mm	50 mm
Stator inner diameter (D_i)	167 mm	27.5 mm
Number of strands (ns)	5	1
Copper fill factor (ff)	44 %	40 %
PM material	N35UH	Recoma26
Insulation Class	180 °C (H)	180 °C (H)
Rated Speed (n_n)	350 rpm	2500 rpm

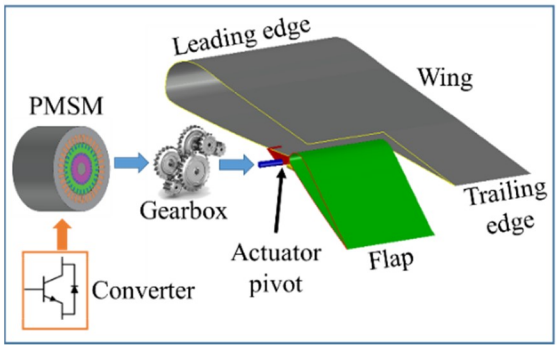

Fig. 3. *Simplified diagram of flap control EMA using Machine A.*

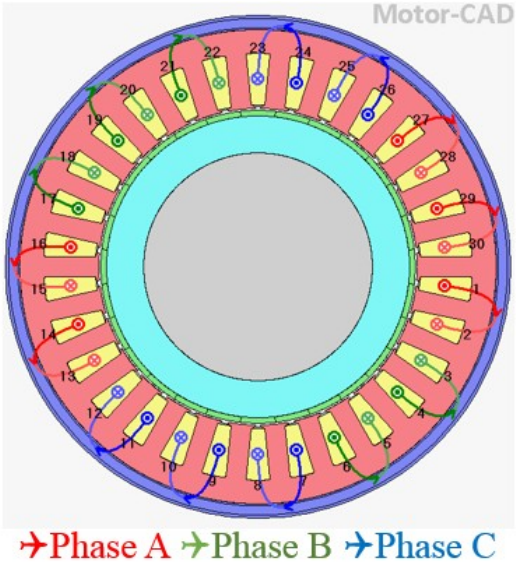

Fig. 4. *Geometry and winding layout of Machine A.*

2.2. Machine B

The PMSM, identified as *Machine B*, is a 12 slots and 10 poles motor, employing a double three-phase CW-AT configuration. The double three-phase winding increases the EMA reliability and availability, because its inherent redundancy allows to avoid single point of failures. The PMSM is meant for a helicopter nose landing gear extension/retraction EMA and the application's functional diagram is delineated in Fig. 5. Each set of three-phase

windings is sized for producing the rated torque of 1 Nm, while 780 Nm are required at the landing gear pivot. Therefore, a gearbox with a 960:1 step-down ratio and 80% efficiency forms the EMA drivetrain. As for *Machine A*, *Machine B* parameters are listed in Table 1, while its geometry is depicted in Fig. 6, together with the windings layout.

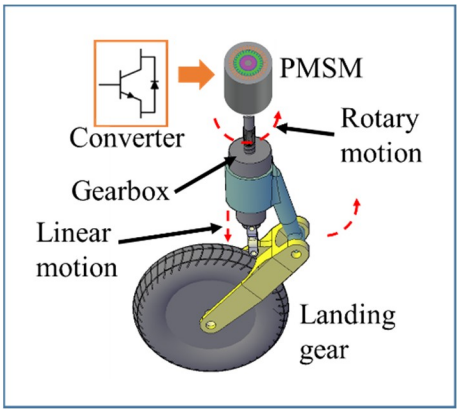

Fig. 5. *Simplified diagram of helicopter landing gear EMA mounting Machine B.*

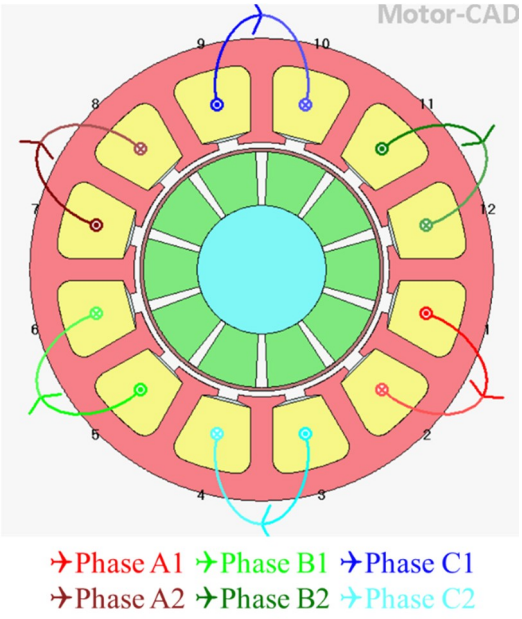

Fig. 6. *Geometry and winding layout of Machine B.*

2.3. Considerations on cooling systems

Although liquid cooled PMSMs can reach higher torque density values compared to the air cooled ones [6, 19, 24], it is desirable to avoid complex cooling infrastructure for aerospace EMA applications [8]. For this reason, the designed PMSMs are naturally air-cooled and the heat generated is dissipated through the finned aluminium housing. It is important to note that the examined applications are mainly driven by short-time duty-cycles. Therefore, these PMSMs are not expected to attain the steady-state temperature at any point in time during the actual operations.

3. PMSMs thermal analysis by LPTN

Thermal models are used for predicting the temperature distribution, in order to evaluate the machines' thermal behaviour. Several methods, such as Computational Fluid Dynamics (CFDs), Finite-Element (FE) and LPTNs, can be adopted for the purpose. In this work, the LPTN is preferred, due to its lower computational time and good accuracy [22, 25].

Preliminary thermal simulations were performed using the commercial software MotorCAD®, for identifying the PMSMs hot-spot and assessing the temperature distribution within the machines. According to the preliminary study findings, the temperature hot-spot is located in the stator windings for both the PMSMs. In addition, electromagnetic FE simulations were carried out in ANSYS® Maxwell 2D, for determining the iron and the PM losses. For rated operating conditions, the obtained results are summarised in Table 2 for *Machine A* and *B*. According to the electromagnetic FE outcomes, the rotor iron losses are two orders of magnitude lower than the ones in the stator, for both PMSMs. Hence, they can be neglected during the thermal analysis. The adoption of segmented PMs, which shortens the eddy-currents paths, makes the PM losses negligible in the two machines. Since the losses in rotor iron and PMs provide a small contribute to the PMSMs total losses, they are not considered in the LPTN. Furthermore, it is reasonable to assume that the rotor is isothermal (at ambient temperature) throughout the short-time transient loading, given its significant thermal inertia [26]. Thus, the rotor is modelled as a temperature source (i.e. infinite thermal inertia), connected to the stator through thermal resistances representing the airgap. In consideration of the relatively low rated speed of the PMSMs, the heat transfer within the airgap mainly occurs by conduction [27]. By exploiting the stator symmetry, each LPTN models a single slot surrounded by a half tooth on each side and the stator back iron on top [21]. The materials' thermal properties, the geometrical dimensions and the heat transfer coefficients are necessary for building the LPTN. The analogy between electrical and thermal quantities is reported in Table 3.

Table 2 Preliminary results: power losses breakdown and temperature distribution (at 500 s) in healthy conditions

Parameter	Machine A	Machine B
Joule losses	360 W	49.8 W
Stator iron losses	97 W	6.9 W
Rotor iron losses	1.8 W	< 0.1 W
PM losses	1.1 W	0.16 W
Winding temperature rise	34.9 K	29.7 K
Stator iron temperature rise	21.1 K	24.8 K
Rotor iron temperature rise	0.95 K	11.1 K
PM temperature rise	1.8 K	11.3 K

Table 3 Thermal and electrical counterparts

Electrical	Thermal
Voltage [V]	Temperature [K]
Current [A]	Heat [W]
Resistance [Ω]	Resistance [K/W]
Capacitance [F]	Capacitance [J/K]

The thermal resistances accounting for conduction and convection heat transfers are calculated by (1) and (2)

respectively, where l and A are the thermal path length and cross-section area, while k and h are the thermal conductivity and the convection heat transfer coefficients respectively.

$$R_{cond} = \frac{l}{k\,A} \tag{1}$$

$$R_{conv} = \frac{1}{h\,A} \tag{2}$$

Radiation heat transfer is intentionally omitted in this study, because its influence is negligible. In fact, relative low temperatures are commonly measured in short-time duty-cycle applications. Transient thermal behaviour is taken into account by including thermal capacitances in the LPTN. These capacitances model the material thermal inertia and they are determined by (3), where c_p is the specific heat capacity and m is the body mass.

$$C_{th} = c_p\,m \tag{3}$$

In a LPTN, heat sources, temperature sources, thermal resistances and capacitances are connected to thermal nodes (or thermal junction). A node is defined active when heat and/or temperature sources are connected to it. Conversely, the junction is referred as passive, if only thermal resistances and/or capacitances form the thermal node. Following the assumptions previously made, the LPTN general structure for both PMSMs under analysis is shown in Fig. 7.

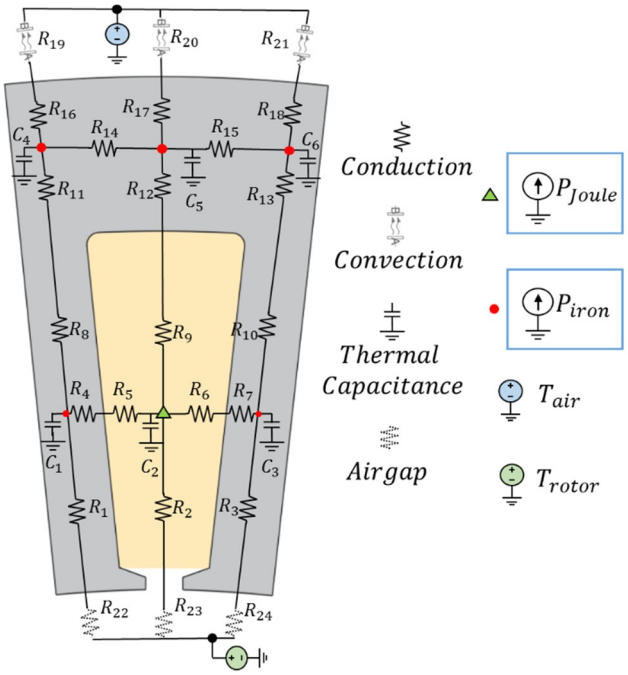

Fig. 7. *LPTN used for performing the thermal analysis of both PMSMs.*

The circumferential heat flow has been considered only in the stator back iron. For sake of clarity, the path of the circumferential heat flow is highlighted in Fig. 8. Replacing (4) and (5) in (1), the circumferential thermal resistances of the stator back iron (i.e. R_{14}, R_{15}) are obtained as in (6).

$$R_{BackIron} = \frac{\varphi}{2k_{iron}L}\frac{ri+ro}{ro-ri} \tag{6}$$

The slot is modelled by radial thermal resistances, which are determined by simplifying the slot geometry to a hexahedron, as depicted in Fig. 9. Introducing the auxiliary variable z (7) and defining the infinitesimal radial resistance (8), the equivalent slot resistances (9) in the radial direction (i.e. R_2, R_9) is determined by integrating (8).

$$z = B1 + \frac{B2-B1}{b}x \tag{7}$$

$$dR_{SlotRad} = \frac{dx}{k_{eq}Lz} \tag{8}$$

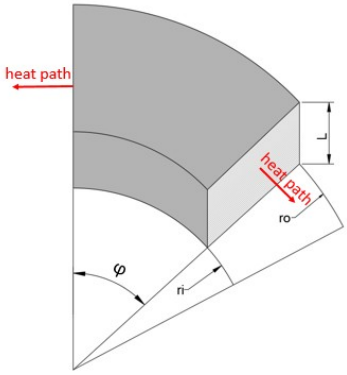

Fig. 8. *Circumferential heat path for stator back iron.*

$$R_{SlotRad} = \int_0^b dR_{SlotRad} = \frac{1}{k_{eq}L}\int_0^b \frac{dx}{\left[B1+\left(\frac{B2-B1}{b}\right)x\right]} \times \frac{\left(\frac{B2-B1}{b}\right)}{\left(\frac{B2-B1}{b}\right)} =$$

$$= \frac{1}{kL\left(\frac{B2-B1}{b}\right)} \times \left\{\ln\left[B1+\left(\frac{B2-B1}{\cancel{b}}\right)\cancel{b}\right] - \ln(B1)\right\} =$$

$$= \frac{1}{kL\left(\frac{B2-B1}{b}\right)} \ln\left(\frac{\cancel{B1}+B2-\cancel{B1}}{B1}\right) \tag{9}$$

From a thermal perspective, the slot can be seen as a compound of two materials, namely copper (conductivity k_{cu}) and impregnating resin plus wire enamel insulation (conductivity k_{res}). Therefore, the value of the equivalent slot thermal conductivity is given by (10).

$$k_{eq} = k_{res}\frac{(1+ff)k_{cu}+(1-ff)k_{res}}{(1-ff)k_{cu}+(1+ff)k_{res}} \tag{10}$$

It is worth pointing out that the thermal conductivity of the wire enamel is similar to the one of impregnating resin; for this reason, they are both accounted through k_{res}. Consequently, ff represents the actual copper fill factor (i.e. ratio between copper surface area and slot surface area). Since the slot liner has a thermal conductivity approaching k_{eq}, its resistance is also included in the slot thermal modelling.

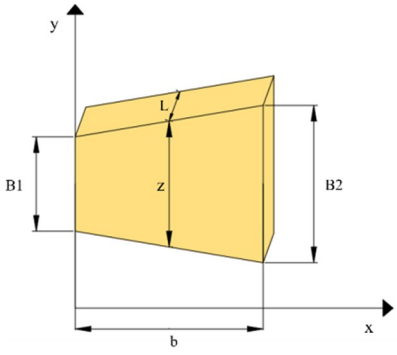

Fig. 9. *Simplified slot shape.*

A similar method is used for determining the equivalent thermal capacitance of the slot. The values of the equivalent slot density and specific heat capacity are expressed by (11) and (12) respectively; where d_{cu} and d_{res} are the copper and resin mass densities, while c_{cu} and c_{res} are the corresponding specific heat capacities.

$$d_{slot} = d_{cu} \times ff + (1 - ff) \times d_{res} \quad (11)$$

$$c_{slot} = c_{cu} \times ff + (1 - ff) \times c_{res} \quad (12)$$

3.1. LPTNs fine-tuning

Accurate temperature estimation can be obtained by using a LPTN. However, there are some critical parameters, which affect the LPTN accuracy and are difficult to be analytically determined. As discussed in [28], some examples of critical parameters are:

- Interference gaps between components;
- Equivalent slot conductivity;
- Convection heat transfer coefficients;
- Uncertainty of material properties.

For most of the critical parameters, their range of variation can be found in literature [29, 30]. These are empirical values based on previous experience and their range might result significantly wide for some of them, as listed in Table 4. Therefore, selecting the appropriate value is not an easy task, also because it will affect the LPTN precision. In order to choose a proper value while still achieving accurate temperature prediction, the critical parameters are experimentally identified.

Table 4 Machines thermal parameters

Parameter	Range [29, 30]	Experimental Machine A	Experimental Machine B
Equivalent Slot conductivity [W/(m·K)]	0.5-2	0.6	0.45
Natural air convection coeff. [W/(m^2·K)]	5-30	12	5
Iron conductivity [W/(m·K)]	25-35	30	30
Equivalent Slot specific heat [J/(kg·K)]	400-1k	430	400
Equivalent Slot mass density [kg/m^2]	4k-5k	4400	4160

An instrumented motorette was manufactured to perform experimental tests on *Machine A*. The motorette consists of six slots with three wound teeth (i.e. CW-AT layout). The three coils are made of class 180 round enamelled magnet wire, with a diameter of 1 *mm*. An enhanced galvanic separation between coils and stator core is provided by a single layer of Nomex paper (i.e. slot liner). The motorette slot fill factor is equal to 0.44 as in the original PMSM. For *Machine B*, the measurements were directly carried out on the actual PMSM, since it was already available and equipped with temperature sensors. The motorette duplicating one tenth of *Machine A*'s stator is shown in Fig. 10 (a), while the complete stator of *Machine B* is depicted in Fig. 10 (b). The winding temperatures are measured by using K-type thermocouples distributed in the coils, and the temperatures are acquired through a data logger. The tests are performed feeding the machines' coils by means of a DC power supply. Although iron losses are neglected during the experimental tests, they have been computed via FE analysis, and included in the LPTNs.

The LPTNs fine tuning has been dealt with the Simulink Design Optimization™ toolbox. In particular, this tool allows to import and pre-process the recorded temperature, and it executes the estimation of the critical thermal parameters by a non-linear least squares optimisation algorithm. Such algorithm aims in minimising the error between the measured temperatures and the ones predicted by the LPTN. Experimental and predicted hot-spot temperatures are evaluated for several DC current values.

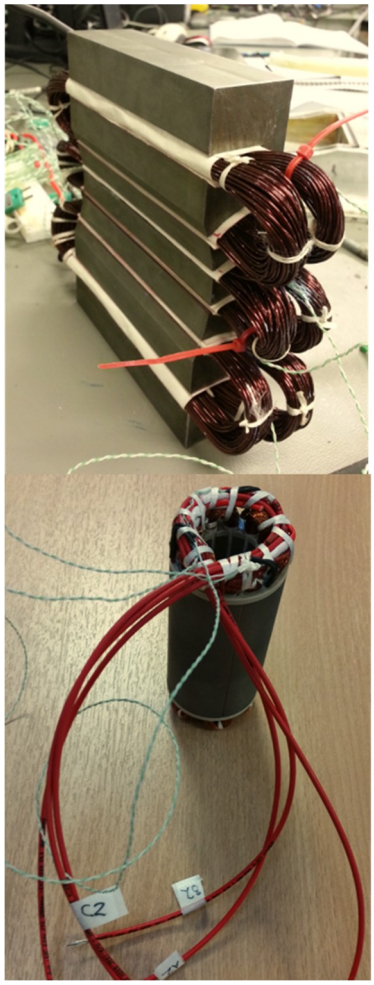

Fig. 10. *Prototypes used for experimental tests:* ***(a)*** *Motorette representing 1/10th of Machine A stator,* ***(b)*** *Complete stator of Machine B.*

In Table 4, the critical parameters (experimentally obtained) are compared to their range of variation proposed in literature, and a good fitting is revealed. The calculated thermal coefficients permit to properly tune the LPTN. The comparison between experimental and LPTN estimated winding temperature profiles (i.e. hot-spot temperature) is reported in Fig. 11, where various current values are considered. In particular, the results regarding *Machine A* and *Machine B* are respectively shown in Fig. 11 (a) and Fig. 11 (b). In the worst-case, the maximum relative error of about 5% is observed. Since both PMSMs are intended for short-time duty-cycle applications (i.e. EMAs), the time window of Fig. 11 is limited to 500 s, which is the most stringent safety constraints required by the two considered EMAs, as detailed in Section 4.3.

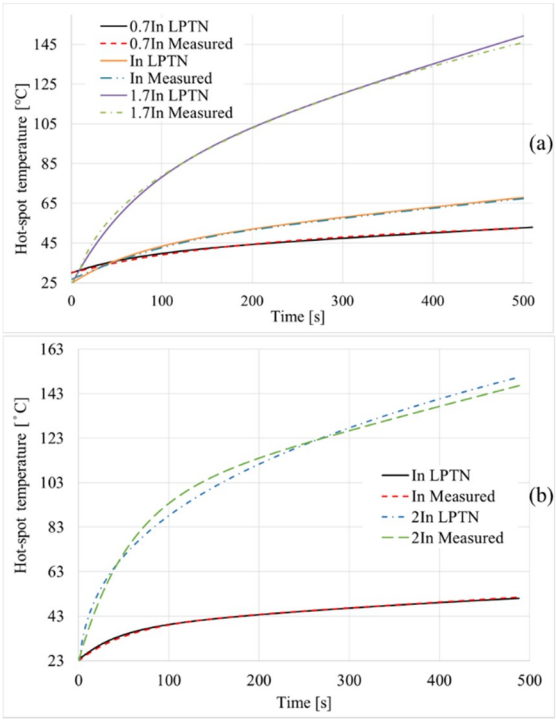

Fig. 11. *Comparison between measured and estimated winding temperature profiles at different current levels:* ***(a)*** *Machine A,* ***(b)*** *Machine B.*

3.2. Considerations and limits of the LPTN

For the sake of fairness, a lower order LPTN (i.e. reduced number of nodes) could have been used for the analysis, due to the short-time duty-cycle of the considered applications. Indeed, the duty-cycle length is more than one order of magnitude lower than the thermal time constant τ (i.e. the time necessary to reach 63.2% of the steady-state temperature) of both *Machine A* and *B*. In particular, *Machine A*'s thermal time constant is approximately 1600 s, whereas the duty-cycle is equal to 60 s (i.e. time for one extension/retraction of the flap EMA). For *Machine B*, the thermal time constant is about 900 s, while its duty-cycle is equal to 20 s (i.e. time for one extension/retraction of the landing gear EMA). Nevertheless, the proposed LPTN structure has general validity and it can be employed for studying the thermal behaviour of machines operating under longer duty-cycles; up to the time interval within the LPTN fine-tuning was performed (i.e. 500 s).

As previously mentioned, the implemented LPTN is built assuming: 1) the PMSM rotor isothermal (i.e. infinite thermal capacitance) and 2) only conductive heat transfer is taken into account within the airgap. However, it is noteworthy that such assumptions affect the accuracy of the steady-state temperature prediction. Indeed, for naturally air cooled machines, a non-negligible portion of heat (produced within the stator) is transferred to the rotor across the airgap. This heat flow is axially extracted from the machine via a low thermal resistance path represented by the rotor shaft. For this reason, the rotor structure needs to be inserted in the LPTN, along with the convective heat transfer in the airgap, when the steady-state temperature evaluation is critical (i.e. continuous running duty).

In the presented modelling procedure, the thermal resistances accounting for the interference gaps between the stator back iron and the frame (i.e. housing), plus the frame thermal resistances have been added in the thermal resistances R_{16}, R_{17} and R_{18}. Similarly, the frame thermal inertia has been deemed by means of the iron thermal capacitances C_4, C_5, and C_6. According to these choices, the temperature distribution in the PMSM frame is not accurate as the one resulting from a LPTN, which separately models both frame and interference gaps thermal resistances. Although the poor estimation on the frame temperature, the proposed LPTN allows to precisely predict the PMSM hot-spot temperature (i.e. winding temperature), as proven by the results shown in Fig. 11. Indeed, this work aims to estimate the winding temperature, which is a critical data, due to the thermal weakness of the insulation system.

4. Machine A: Analysis and EMA case study

In this section, the previously validated and fine-tuned LPTN is adopted for predicting *Machine A*'s thermal behaviour. The thermal analysis is performed considering two operating modes, namely healthy and single-phase open-circuit fault. The control strategy applied after the fault injection is also discussed throughout the section.

4.1. Machine A: Healthy operating condition

In healthy condition, the phase current is equal to 28.3 Arms, which corresponds to a current density of 7.2 A/mm^2. The electrical resistance for determining the copper losses is calculated by (13), where l_{coil} is the length of one turn, N_{turns} is the number of turns, s_{cond} is the cross-section area of the wire and $\rho_{cu}(T)$ is the copper electrical resistivity at temperature T.

$$R_{coil} = \frac{l_{coil} N_{turns}}{s_{cond} \rho_{cu}(T)} \tag{13}$$

Since the resistivity varies with the temperature, it is necessary to iterate the LPTN simulation a few times. This process is automated with a LPTN built in Simscape™ and monitored by a purposely-created Matlab® script. The instantaneous value of the electromagnetic torque is obtained through FE simulation using ANSYS® Maxwell 2D. The developed torque at rated current is equal to 137.13 Nm (average value), as depicted in Fig. 12. Fig. 13 shows the PMSM's flux lines and magnetic flux density at rated and healthy conditions.

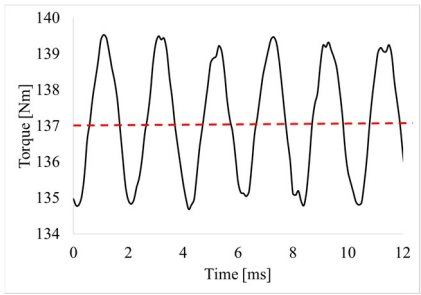

Fig. 12. *Machine A: instantaneous (black continuous line) and average (red dashed line) electromagnetic torque at rated current in healthy condition.*

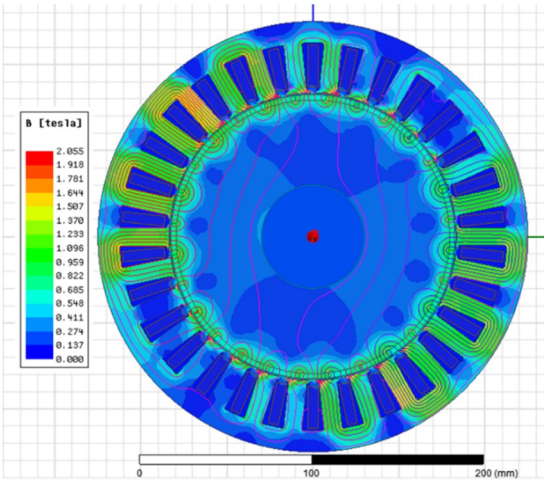

Fig. 13. *Machine A: flux lines and magnetic flux density at rated current in healthy condition.*

As mentioned earlier, the copper losses are calculated analytically, while the stator iron losses are carried out from FE model. These losses are used for feeding the LPTN, which will estimate the winding temperature in both healthy mode and single-phase open-circuit fault. The LPTN ambient temperature is set equal to 70 °C, which considers the worst-case scenario for the aerospace application under study.

4.2. Machine A: Single-phase open-circuit fault

If a single-phase open-circuit fault occurs, a suitable control strategy needs to be implemented for completing the EMA mission. Hence, the required torque should be developed even under fault. Assuming a single-phase open-circuit on the phase 'A', the simplest control strategy consists in increasing the amplitude of the currents flowing through the healthy phases ('B' and 'C') by $\sqrt{3}$ and displacing their vectors by 30 degrees from the original axis position, as illustrated in Fig. 14 [31]. In particular, Fig. 14 reports the developed torque and the control strategy in three different operating modes:

1. From 0 to 50 ms *Machine A* operates at rated current with the three phases normally fed.
2. At 50 ms the phase 'A' is open to simulate the fault. Thus, from 50 to 100 ms, *Machine A* works with one phase open and the compensation strategy is not applied yet.
3. At 100 ms the compensation strategy is activated. Therefore, *Machine A* generates the rated torque despite the faulty phase, from 100 to 150 ms.

Adopting the described control strategy, the PMSM is able to develop 135.45 Nm (average torque), albeit the open phase. This average torque satisfies the application requirement allowing the EMA mission accomplishment. However, the PMSM torque ripple increases compared to the healthy case. Table 5 summarizes the average torque and the torque ripple values, during pre- and post- fault conditions (with and without control strategy). The ratio between actual and rated phase current (I_{ph}/I_n) is also listed in the table. It is worth pointing out that the power converter must be designed to handle the overload condition (i.e. 173% of the rated current), for avoiding further faults after the control strategy activation.

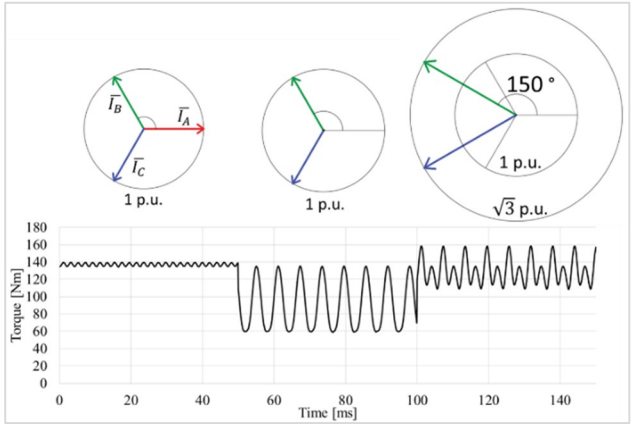

Fig. 14. *Machine A: torque and control strategy pre- and post-fault.*

Table 5 PMSM performance pre- and post- single-phase open-circuit

Operating Condition	T_{avg} *[Nm]*	*ripple*	I_{ph}/I_n
Healthy (0-50 ms)	137.13	3.5 %	1
Faulty (50-100 ms)	92.36	82.1 %	1
Control Strategy (100-150 ms)	135.45	38.6 %	1.73

4.3. Machine A: Thermal analysis during mission profile

Analysed *Machine A* performance, the fine-tuned LPTN is finally used for estimating the winding temperature in healthy and faulty modes. On the other hand, the validated LPTN might also be employed for defining the maximum torque profile achievable, without exceeding the insulation thermal class (i.e. 180 °C). As previously mentioned, *Machine A* is integrated on EMA, which drives the flap of a medium sized civil aircraft. Flaps are secondary flight controls and they increase the aircraft wing's lift during take-off and landing. Hence, the flap EMA is operated only for a small fraction of the total flight time. For a medium sized civil aircraft, the time necessary for flap extension (or retraction) is usually less than 30 s. However, for safety reasons, the PMSM must be able to perform three complete cycles (extension + retraction) every 500 s with a rest time of 60 s between each cycle [23]. The aforementioned flap mission profile is provided in Fig. 15 [23], alongside with the PMSM torque profile duty-cycle.

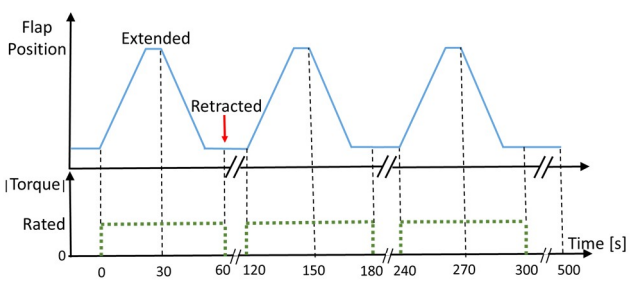

Fig. 15. *Flap mission profile (blue continuous line) and PMSM torque profile duty-cycle (green dashed line).*

The predicted winding temperature profiles, considering the flap EMA mission in both healthy and faulty operating conditions, are displayed in Fig. 16

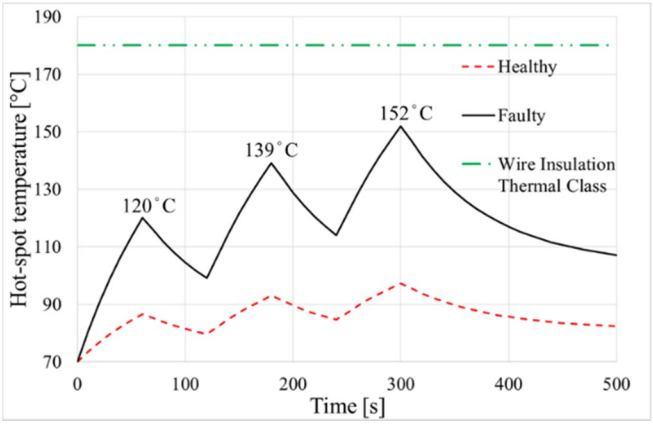

Fig. 16. *Machine A winding temperature profiles in healthy and fault conditions during EMA mission.*

The obtained results show how *Machine A* can work even in case of single-phase open-circuit, without exceeding the thermal class of the wire insulation (green line in Fig. 16). In fact, the highest temperature reached throughout the flap EMA duty-cycle (i.e. 152 °C) is well below the maximum allowable temperature of 180°C. Therefore, the insulation system lifetime is not compromised by the single-phase open-circuit fault and the consequent control strategy implementation.

5. Machine B: Analysis and EMA case study

Similarly to the analysis carried out in Section 4 for *Machine A*, the electromagnetic performance and the thermal behaviour of *Machine B* are here investigated for several operating modes. Additionally, considerations regarding the post-fault control strategy are given. The thermal analysis is performed using the experimentally validated LPTN, while the FE simulations are adopted for evaluating the electromagnetic capability. The healthy case and the three-phase short-circuit in one star are considered for *Machine B*, whose winding is a double three-phase. Despite its low occurrence probability compared to other winding faults (e.g. turn-to-turn and/or phase-to-ground short circuits), the whole short-circuit of one three-phase winding is studied, due to its inherent feature of being a symmetric fault. Indeed, three-phase short-circuit may intentionally be induced in response to an asymmetric fault detection, in order to reduce the torque oscillations, which may cause mechanical failures of the drive-train [32].

5.1. Machine B: Healthy operating condition

As earlier introduced, *Machine B* is equipped with a double three-phase winding for redundancy purposes. Further, the landing gear EMA safety requirements are fulfilled by designing each winding set for delivering 1 Nm (rated torque). For sake of completeness, the instantaneous torque generated by *Machine B* is reported in Fig. 17. In healthy mode, the double three-phase winding can be fed in two different ways for developing the rated torque. The first approach consists in supplying only one three-phase winding at rated current (i.e. 2.2 Arms), while the second set is open. Alternatively, 1 Nm torque is also produced, when both the three-phase windings are simultaneously fed with half of the rated current (i.e. 1.1 Arms). For the described methods, the flux density distribution is shown in Fig. 18 and Fig. 19 respectively. As expected, a higher saturation level is observable within the stator teeth, when only one three-phase winding is powered.

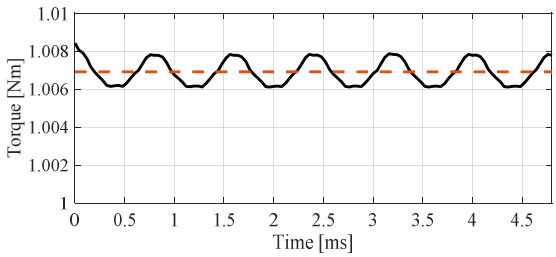

Fig. 17. *Machine B: instantaneous (black continuous line) and average (red dash line) electromagnetic torque in healthy condition.*

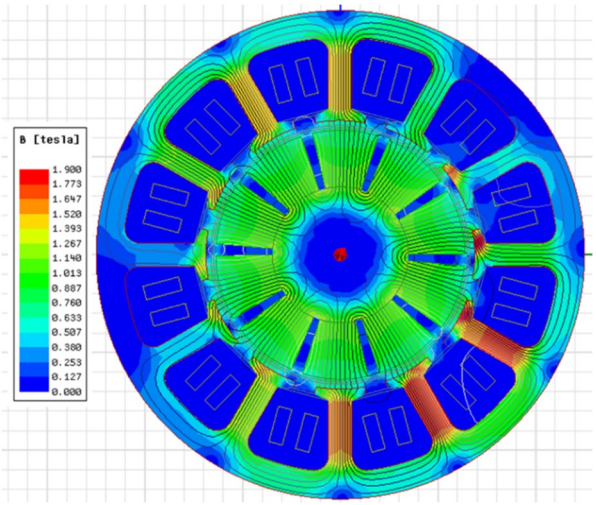

Fig. 18. *Machine B: flux lines and magnetic flux density when only one three-phase winding is fed with 2.2 Arms current (healthy condition).*

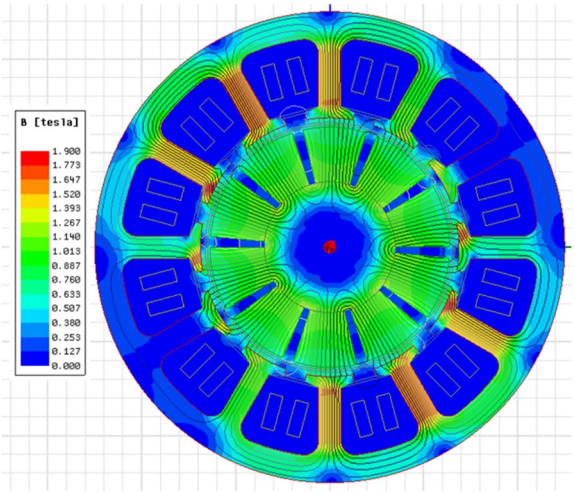

Fig. 19. *Machine B: flux lines and magnetic flux density when both three-phase windings are simultaneously fed with 1.1 Arms current (healthy condition).*

Although the two operating modes are equivalent in terms of torque, the amount of Joule losses generated within the windings is different. In particular, when only one three-phase winding is supplied at the rated current, the *Machine B*'s Joule losses are doubled compared to when the rated current is split between the two winding sets. Hence, the former operating mode is more thermally challenging, due to the higher amount of heat to be extracted. For this reason, the LPTN investigation will be performed considering the whole rated current applied to one three-phase winding, as healthy condition.

5.2. Machine B: Short-circuit of one three-phase winding

Machine B can drive the landing gear EMA even in case of severe windings or converters faults. In terms of thermal loading, the most challenging fault is represented by the complete short-circuit of one winding set. In fact, the short-circuited winding develops a braking torque, which depends on the PMs speed. For *Machine B*, the braking torque trend as function of the rotor speed has been determined by FE simulations and experimentally. The obtained results are reported in Fig. 20.

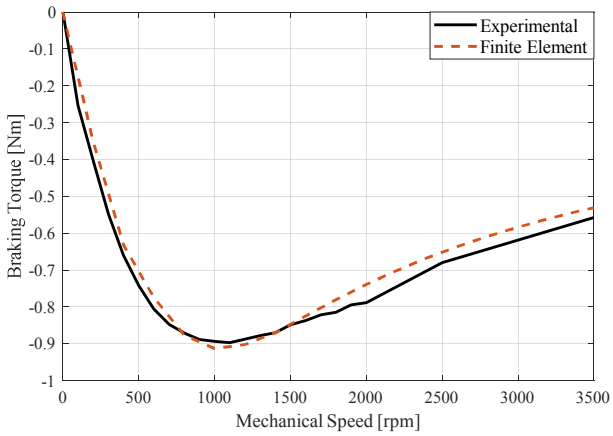

Fig. 20. *Braking torque developed by the Machine B when one of the two stars is short-circuited.*

From Fig. 20, the maximum absolute value of braking torque (i.e. -0.913 Nm) is reached at 1000 rpm, whereas at rated speed (i.e. 2500 rpm), a braking torque of -0.652 Nm is delivered. Therefore, the healthy winding is thermally more stressed, when the three-phase short-circuit occurs at 1000 rpm (i.e. worst-case possible). Indeed, the healthy winding should provide an overall torque of 1.913 Nm, which is sum of the two terms:

a) the rated torque (i.e. 1 Nm), for completing the landing gear EMA mission;
b) the torque necessary, for compensating the braking torque (i.e. -0.913 Nm at 1000 rpm).

In order to produce 1.913 Nm, a current of 4.47 Arms (about twice the rated current) needs to flow through the healthy winding. Thus, *Machine B*'s control strategy consists in increasing the current in the healthy winding, according to the braking torque value. In Fig. 21, the electromagnetic torque and the phase currents in both three-phase windings are shown for three operating conditions at 1000 rpm.

1) From 0 to 24 ms, *Machine B* operates in healthy condition developing 1 Nm and both windings are fed with half rated current (i.e. 1.1 Arms). As highlighted in Fig. 21 (top sub-plot), the torque ripple is negligible (i.e. 0.23%).
2) At 24 ms, a three-phase short-circuit is injected in one winding, while the current in the other winding is kept equal to 1.1 Arms. Therefore, from 24 to 60 ms, the *Machine B* works under fault condition without compensation strategy. The torque at the PMSM shaft is equal to -0.408 Nm (this value will compromise the landing gear EMA mission), whilst 2.74 Arms flow through the short-circuited winding (middle sub-plot).
3) At 60 ms, the compensation strategy is implemented by increasing the current in the healthy winding from 1.1 Arms to 4.47 Arms (bottom sub-plot). Hence, *Machine B* delivers 1.01 Nm (average torque) with 3.35% ripple, from 60 to 83 ms despite the fault.

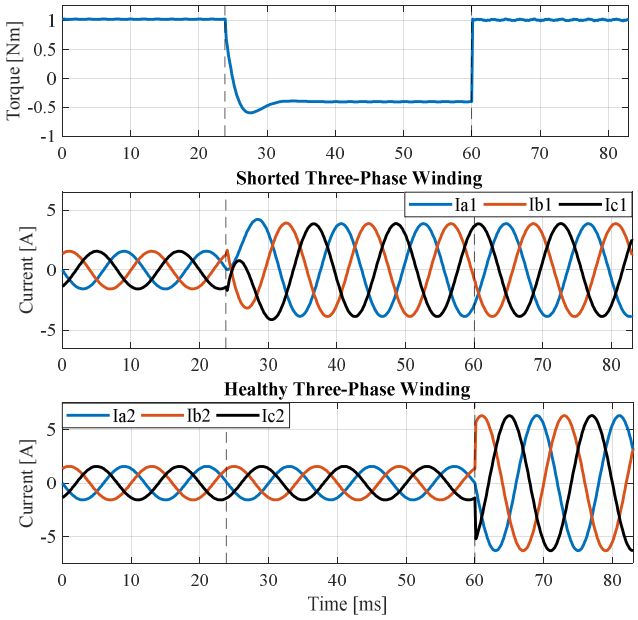

Fig. 21. *Torque and phase currents (in both three-phase windings) in Machine B during a) healthy condition (0-24 ms), b) three-phase short-circuit of one winding (24-60 ms) and c) compensation strategy implementation (60-84 ms).*

In the next sub-section, *Machine B*'s winding temperatures are predicted by the fine-tuned LPTN, in healthy and faulty conditions. For each operating mode, the most challenging case will be considered.

5.3. Machine B: Thermal analysis and mission profile

The helicopter landing gear EMA is characterised by a short-time duty-cycle. The time necessary for a single extraction/retraction cycle is equal to 20 s. For safety reasons, three complete extraction/retraction cycles in a row must be performed, without any cooling-down time. In other words, the rated torque (i.e. 1 Nm) needs to be developed continuously for 60 s. During this time-span, the winding temperature should not exceed the insulation thermal class

(i.e. 180°C), in order to avoid unwanted aging. The fine-tuned LPTN is employed for estimating the winding temperature in the following operating conditions:

a) only one three-phase winding is fed with the rated current (i.e. healthy condition);
b) three-phase short-circuit at 1000 rpm (i.e. faulty condition).

For the thermal simulations, the initial temperature is set equal to 70°C (i.e. maximum expected ambient temperature). The obtained results are given in Fig. 22, where the temperature profile of the winding is predicted a) at rated current and b) when the compensation strategy is applied for a three-phase short-circuit at 1000 rpm. As for the previous study case, even for *Machine B*, the maximum winding temperature is well below the insulation thermal class. This outcome is in line with the general rule of thumb, whereby a safety margin needs to be included, since the location of the highest temperature can never be identified exactly. For the specific application, the safety margin accounts also for the temperature raise, due to the heat generated by the short-circuited winding.

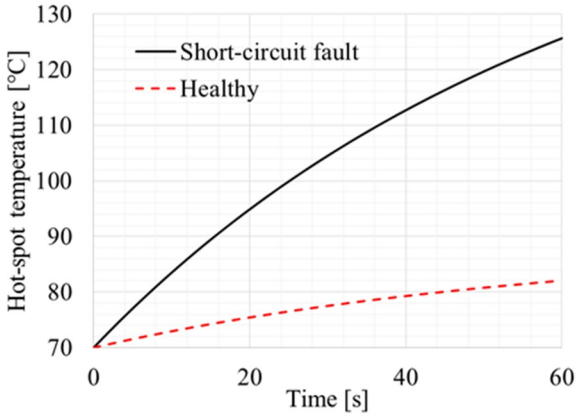

Fig. 22. *Machine B: winding temperature profiles in healthy and fault conditions, during landing gear EMA mission.*

6. Conclusions

In this paper two fault-tolerant PMSMs for aerospace applications have been investigated with special target on their thermal behaviour in both healthy and faulty conditions. This work focuses its attention on the importance of including the thermal analysis at the design stage of fault-tolerant PMSMs. Indeed, for safety-critical applications, the electrical machine must be able to withstand the increased thermal loading arising from the implementation of post-fault compensation strategy. The architecture of the LPTN used for the thermal analysis is presented and discussed. Better accuracy in temperature prediction is achieved by experimentally fine-tuning the LPTN. The fine-tuning process allows to identify the LPTN critical parameters, such as equivalent slot conductivity, convection heat transfer coefficient, etc..., which would otherwise be difficult to be analytically determined. Two study cases, namely a civil aircraft flap EMA and a helicopter landing gear EMA, are considered for proving the PMSMs capability of working safely under fault conditions, without exceeding the insulation thermal class. The provided considerations regarding the thermal modelling and the control strategy in faulty operations have general validity. Thus, they can be extended to different machine topologies and applications.

7. Acknowledgements

This work was funded by the INNOVATIVE doctoral programme. The INNOVATIVE programme is partially funded by the Marie Curie Initial Training Networks (ITN) action (project number 665468) and partially by the Institute for Aerospace Technology (IAT) at the University of Nottingham.

This work was also partially funded by the University of Nottingham Propulsion Futures Beacon.

8. References

[1] C. I. Hill, S. Bozhko, Y. Tao, P. Giangrande, and C. Gerada, "More Electric Aircraft Electro-Mechanical Actuator Regenerated Power Management," in *2015 IEEE 24th International Symposium on Industrial Electronics (ISIE)*, 2015, pp. 337-342.

[2] V. Madonna, P. Giangrande, and M. Galea, "Electrical Power Generation in Aircraft: review, challenges and opportunities.," *in press on IEEE Transactions on Transportation Electrification,* DOI: 10.1109/TTE.2018.2834142, 2018.

[3] J. A. Rosero, J. A. Ortega, E. Aldabas, and L. Romeral, "Moving towards a more electric aircraft," *IEEE Aerospace and Electronic Systems Magazine,* vol. 22, pp. 3-9, 2007.

[4] P. Giangrande, F. Cupertino, and G. Pellegrino, "Modelling of linear motor end-effects for saliency based sensorless control," in *2010 IEEE Energy Conversion Congress and Exposition*, 2010, pp. 3261-3268.

[5] R. Glassock, M. Galea, W. Williams, and T. Glesk, "Novel Hybrid Electric Aircraft Propulsion Case Studies," *Aeronautics and Astronautics, MDPI Journal on,* vol. vol. 4, iss. 3, article 45, 2017.

[6] A. Al-Timimy, M. Degano, P. Giangrande, G. L. Calzo, Z. X. M. Galea, C. Gerada*, et al.*, "Design and optimization of a high power density machine for flooded industrial pump," in *2016 XXII International Conference on Electrical Machines (ICEM)*, 2016, pp. 1480-1486.

[7] C. Sciascera, P. Giangrande, C. Brunson, M. Galea, and C. Gerada, "Optimal design of an electro-mechanical actuator for aerospace application," in *IECON 2015 - 41st Annual Conference of the IEEE Industrial Electronics Society*, 2015, pp. 001903-001908.

[8] C. Gerada, M. Galea, and A. Kladas, "Electrical machines for aerospace applications," in *2015 IEEE Workshop on Electrical Machines Design, Control and Diagnosis (WEMDCD)*, 2015, pp. 79-84.

[9] F. Cupertino, P. Giangrande, L. Salvatore, and G. Pellegrino, "Model based design of a sensorless control scheme for permanent magnet motors using signal injection," in *2010 IEEE Energy Conversion Congress and Exposition*, 2010, pp. 3139-3146.

[10] D. Barater, F. Immovilli, A. Soldati, G. Buticchi, G. Franceschini, C. Gerada*, et al.*, "Multistress Characterization of Fault Mechanisms in Aerospace Electric Actuators," *IEEE Transactions on Industry Applications,* vol. 53, pp. 1106-1115, 2017.

[11] B. C. Mecrow, A. G. Jack, J. A. Haylock, and J. Coles, "Fault-tolerant permanent magnet machine drives," *IEE Proceedings - Electric Power Applications,* vol. 143, pp. 437-442, 1996.

[12] P. Giangrande, C. I. Hill, S. V. Bozhko, and C. Gerada, "A novel multi-level electro-mechanical actuator virtual testing and analysis tool," in *7th IET International Conference on Power Electronics, Machines and Drives (PEMD 2014)*, 2014, pp. 1-6.

[13] D. Ishak, Z. Q. Zhu, and D. Howe, "Comparison of PM brushless motors, having either all teeth or alternate teeth wound," *IEEE Transactions on Energy Conversion,* vol. 21, pp. 95-103, 2006.

[14] S. A. Odhano, P. Giangrande, R. Bojoi, and C. Gerada, "Self-commissioning of interior permanent magnet synchronous motor drives with high-frequency current injection," in *2013 IEEE Energy Conversion Congress and Exposition*, 2013, pp. 3852-3859.

[15] A. G. Jack, B. C. Mecrow, and J. A. Haylock, "A comparative study of permanent magnet and switched reluctance motors for high-performance fault-tolerant applications," *IEEE Transactions on Industry Applications,* vol. 32, pp. 889-895, 1996.

[16] N. Bianchi, S. Bolognani, M. D. Pre, and E. Fornasiero, "Post-fault operations of five-phase motor using a full-bridge inverter," in *2008 IEEE Power Electronics Specialists Conference*, 2008, pp. 2528-2534.

[17] N. Bianchi, M. D. Pre, G. Grezzani, and S. Bolognani, "Design considerations on fractional-slot fault-tolerant synchronous motors," in *IEEE International Conference on Electric Machines and Drives, 2005.*, 2005, pp. 902-909.

[18] A. Al-Timimy, P. Giangrande, M. Degano, M. Galea, and C. Gerada, "Comparative study of permanent magnet-synchronous and permanent magnet-flux switching machines for high torque to inertia applications," in *2017 IEEE Workshop on Electrical Machines Design, Control and Diagnosis (WEMDCD)*, 2017, pp. 45-51.

[19] Z. Xu, A. Al-Timimy, M. Degano, P. Giangrande, G. L. Calzo, H. Zhang*, et al.*, "Thermal management of a permanent magnet motor for an directly coupled pump," in *2016 XXII International Conference on Electrical Machines (ICEM)*, 2016, pp. 2738-2744.

[20] C. Sciascera, M. Galea, P. Giangrande, and C. Gerada, "Lifetime consumption and degradation analysis of the winding insulation of electrical machines," in *8th IET International Conference on Power Electronics, Machines and Drives (PEMD 2016)*, 2016, pp. 1-5.

[21] C. Sciascera, P. Giangrande, L. Papini, C. Gerada, and M. Galea, "Analytical Thermal Model for Fast Stator Winding Temperature Prediction," *IEEE Transactions on Industrial Electronics,* vol. 64, pp. 6116-6126, 2017.

[22] A. Boglietti, A. Cavagnino, D. Staton, M. Shanel, M. Mueller, and C. Mejuto, "Evolution and Modern Approaches for Thermal Analysis of Electrical Machines," *IEEE Transactions on Industrial Electronics,* vol. 56, pp. 871-882, 2009.

[23] J. W. Bennett, B. C. Mecrow, A. G. Jack, and D. J. Atkinson, "A Prototype Electrical Actuator for Aircraft Flaps," *IEEE Transactions on Industry Applications,* vol. 46, pp. 915-921, 2010.

[24] A. Al-Timimy, M. Degano, Z. Xu, G. L. Calzo, P. Giangrande, M. Galea*, et al.*, "Trade-off analysis and design of a high power density PM machine for flooded industrial pump," in *IECON 2016 - 42nd Annual Conference of the IEEE Industrial Electronics Society*, 2016, pp. 1749-1754.

[25] M. Galea, C. Gerada, T. Raminosoa, and P. Wheeler, "A Thermal Improvement Technique for the Phase Windings of Electrical Machines," *IEEE Transactions on Industry Applications,* vol. 48, pp. 79-87, 2012.

[26] A. Boglietti, E. Carpaneto, M. Cossale, and S. Vaschetto, "Stator-Winding Thermal Models for Short-Time Thermal Transients: Definition and Validation," *IEEE Transactions on Industrial Electronics,* vol. 63, pp. 2713-2721, 2016.

[27] A. Boglietti, E. Carpaneto, M. Cossale, and A. L. Borlera, "Stator thermal model for short-time thermal transients," in *2014 International Conference on Electrical Machines (ICEM)*, 2014, pp. 1415-1421.

[28] A. Boglietti, A. Cavagnino, and D. Staton, "Determination of Critical Parameters in Electrical Machine Thermal Models," *IEEE Transactions on Industry Applications,* vol. 44, pp. 1150-1159, 2008.

[29] W. Tong, *Mechanical Design of Electric Motors*: Taylor & Francis, 2014.

[30] J. Pyrhonen, T. Jokinen, and V. Hrabovcova, *Design of rotating electrical machines*: John Wiley & Sons, 2009.

[31] B. A. Welchko, T. A. Lipo, T. M. Jahns, and S. E. Schulz, "Fault tolerant three-phase AC motor drive topologies: a comparison of features, cost, and limitations," *IEEE Transactions on Power Electronics,* vol. 19, pp. 1108-1116, 2004.

[32] B. A. Welchko, T. M. Jahns, W. L. Soong, and J. M. Nagashima, "IPM synchronous machine drive response to symmetrical and asymmetrical short circuit faults," *IEEE Transactions on Energy Conversion,* vol. 18, pp. 291-298, 2003.